Supplementary Material for on-line publication only

New insights into the alkoxy effects on auxiliary adsorption and inhibiting charge recombination in dye-sensitized solar cells with high open circuit voltage: a theoretical investigation

Zi-han Xu, [a] Chang-yan Zhu, [c] Xiao-fei Zhu, [a] Yu-juan Zhai, [a] Ji Zhang, [*a] Han-cheng Zhu[*b]

[a] School of Chemistry and Life Science, Changchun University of Technology, Changchun 130012, Jilin, P. R. China.
[b] Key Laboratory of UV-Emitting Materials and Technology, Northeast Normal University, Ministry of Education, Changchun 130024, China.
[c] Institute of Functional Material Chemistry, School of Chemistry, Northeast Normal University, Changchun 130024, Jilin, P. R. China.

[*]Corresponding author: Ji Zhang: zhangj158@ccut.edu.cn;

Han-cheng Zhu: zhuhc@nenu.edu.cn

1. Computational Details about the molecular configuration search the optimization of dye@TiO$_2$ systems

Here, Molclus combined with XTB were used for the molecular configuration search of the ullazine dyes with long alkoxy chain. Molclus is a free, flexible and easy-to-use molecular configuration search program developed by Lu Tian. [1] XTB [2] is a program developed by Grimme specifically for GFN-XTB (Geometry, Frequency, Noncovalent, eXtended TB) calculation. [3, 4] (1) First, run the dynamics with XTB under GFN0-xTB. The temperature is set to 500K. The total simulation time is 200ps. Write it into the track file every 50fs. Restrict the chemical bond distance related to hydrogen with shake algorithm. A total of 4000 configurations are saved in the track file; (2) the 4000 configurations were optimized with GFN0-xTB using crest program, then the Isostat tool in the Molclus program was carried out for the energy ranking and deleting the duplicated structures (3) these configurations without duplicated structures were further optimized with GFN2-xTB using crest program under the dichloromethane solvent model, [5-7] then Isostat tool is used again for the energy ranking and deleting the duplicated structures, the first 20 configurations with the lowest energy are retained; (4) geometric optimization and vibration analysis were carried out under vacuum for these 20 configurations with B3LYP-D3(BJ)/6-311G** as implemented in Gaussian 16; (5) based on the optimized structures of the first 20 configurations, single point energy were performed with PWPB95-D3(BJ)/def2-TZVPP [8-10] combined with SMD model, [11] as implemented in ORCA (revision 4.2) program; [12-14] (5) at last, Gibbs free energy in solution and the Boltzmann distribution at 298.15K for these 20 configurations were calculated by Shermo program. [15] Here quasi-RRHO (rigid-rotor harmonic oscillator) model proposed by Grimme were used to consider the contribution of the internal motion of the system to the thermodynamic quantity. [16]

In order to investigate the alkoxy effects on the adsorption of dyes on the TiO$_2$ surface, the (TiO$_2$)$_{82}$ cluster (Fig.S1), cutting an anatase slab to expose the majority (101) surface as proposed by Persson et al [17] and De Angelis et al, [18] were used to model the TiO$_2$ nanoparticle effects. The dye@(TiO$_2$)$_{82}$ complexes with different adsorption configurations were optimized by the SIESTA program, [19-21] employing the generalized gradient approximation (GGA) of the

Perdew−Burke−Ernzerhof (PBE) [22] functional in conjunction with DZP Slater-type basis sets. During the optimization, a dispersion potential of the Grimme type were added to describe the weak interaction. [23] Additionally, the reliability of the approach discussed above has already been proven by multiple studies. [24-32]
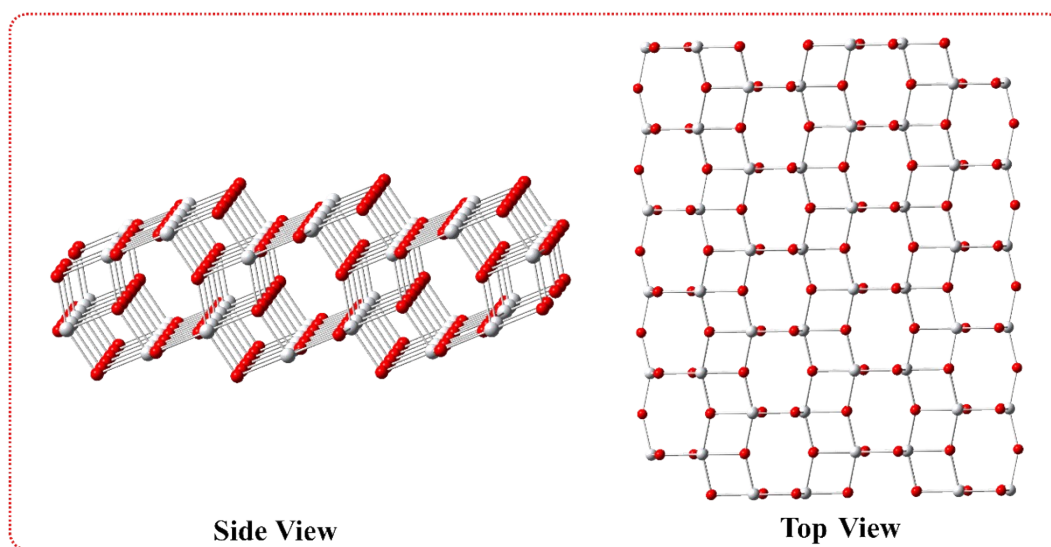

Fig. S1 Initial structure of $(TiO_2)_{82}$ cluster in side and top view.

2. Details about the reduced density gradient (RDG) analysis and independent gradient model based on Hirshfeld partition (IGMH) analyses

Reduced density gradient (RDG) method proposed by Yang et al. [33] were used to visualize weak intramolecular interaction. The definition of the RDG function is shown below:

$$RDG(r) = \frac{1}{2(3\pi^2)^{1/3}} \frac{|\nabla\rho(r)|}{\rho(r)^{4/3}} \tag{1}$$

Here, $\nabla\rho(r)$ is electron density gradient. Then, a real space function $sign(\lambda_2)\rho$ can be mapped on the RDG isosurface by different colors to visually characterize the nature of the interactions as the color bar shown in Fig.3. Here, $sign(\lambda_2)$ means the sign of the second largest eigenvalue of electron density Hessian matrix at position r. According to the color-filled RDG map, we can not only know where weak interaction occurs, but also intuitively capture the type of the

interaction.

Independent gradient model based on Hirshfeld partition (IGMH) analyses in Multiwfn were carried out for the visual study of interactions between the adsorbed sensitizer and the TiO_2 surface [34]. IGMH analyses is based on the discussion of δg, which is a real three-dimensional real space function and could clearly display the interaction region between atoms. The stronger the interaction between atoms, the larger the δg in the interaction region. δg is defined as the difference between two density gradients, that is the independent gradient based on Hirshfeld partition (g^{IGMH}) and gradient of promolecular density (g)

$$\delta g(r) = g^{IGMH}(r) - g(r) \tag{2}$$

$$g^{IGMH}(r) = \sum \left| \nabla \rho_i^{Hirsh}(r) \right| \tag{3}$$

$$g(r) = \left| \sum_i \nabla \rho_i^{Hirsh}(r) \right| \tag{4}$$

where r denotes Cartesian coordinate vector, i loops over all atoms. ρ_i^{Hirsh} is the atomic density based on Hirshfeld partition, and can be defined as the product of actual electron density calculated by quantum chemistry method (ρ) and the Hirshfeld weighting function of the atom i (w_i)

$$\rho_i^{Hirsh}(r) = \rho(r)w_i(r) \tag{5}$$

with

$$w_i(r) = \frac{\rho_i^{free}(r)}{\rho^{pro}(r)} = \frac{\rho_i^{free}(r)}{\sum_j \rho_j^{free}(r)} \tag{6}$$

Here, ρ_i^{free} is the free-state atomic density. Then, the gradient of Hirshfeld atomic density $\nabla \rho_i^{Hirsh}$ can be calculated:

$$\nabla \rho_i^{Hirsh} = \frac{\partial \rho_i^{Hirsh}}{\partial \mu} = \frac{\partial(\rho w_i)}{\partial \mu} = w_i \frac{\partial \rho}{\partial \mu} + \rho \frac{\partial w_i}{\partial \mu} = \frac{\rho_i^{free}}{\rho^{pro}} \frac{\partial \rho}{\partial \mu} + \frac{\rho}{\rho^{pro}} \frac{\partial \rho_i^{free}}{\partial \mu} - \frac{\rho \rho_i^{free}}{(\rho^{pro})^2} \sum_j \frac{\partial \rho_i^{free}}{\partial \mu} \tag{7}$$

And μ is the Cartesian coordinate component

Then, δg can be divided into δg^{intra} used to show the interaction within fragment and δg^{inter} used to show the interaction between fragment. Here we focus on the $\delta g^{int\,er}$. It is defined as below:

$$\delta g^{int\,er}(r) = g^{IGM,int\,er}(r) - g^{int\,er}(r) \qquad (8)$$

with

$$g^{int\,er}(r) = \left| \sum_A \sum_{i \in A} \nabla \rho_i^{Hirsh}(r) \right| \qquad (9)$$

$$g^{IGM,int\,er}(r) = \sum_A \left| \sum_{i \in A} \nabla \rho_i^{Hirsh}(r) \right| \qquad (10)$$

A represents the fragment and i represents the atom in the fragment.

Then, the real space function $sign(\lambda_2)\rho$ can be mapped on the isosurface of δg^{inter} by different colors to visually characterize the nature of the interactions as the color bar shown in Fig. S2.
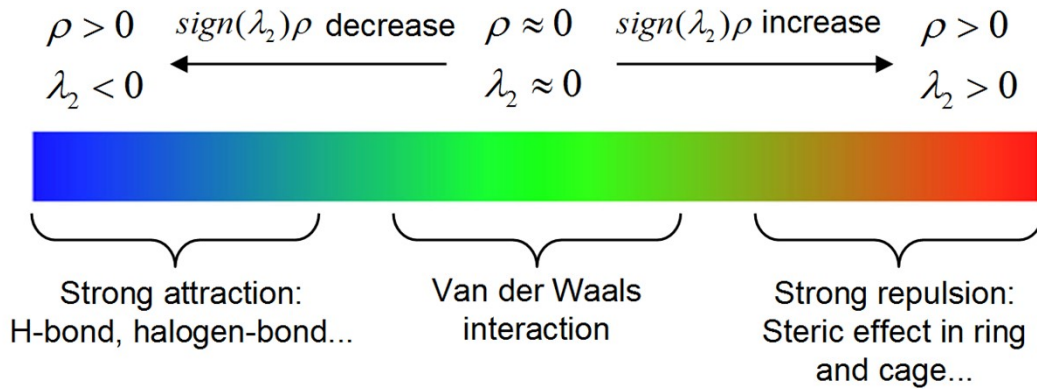

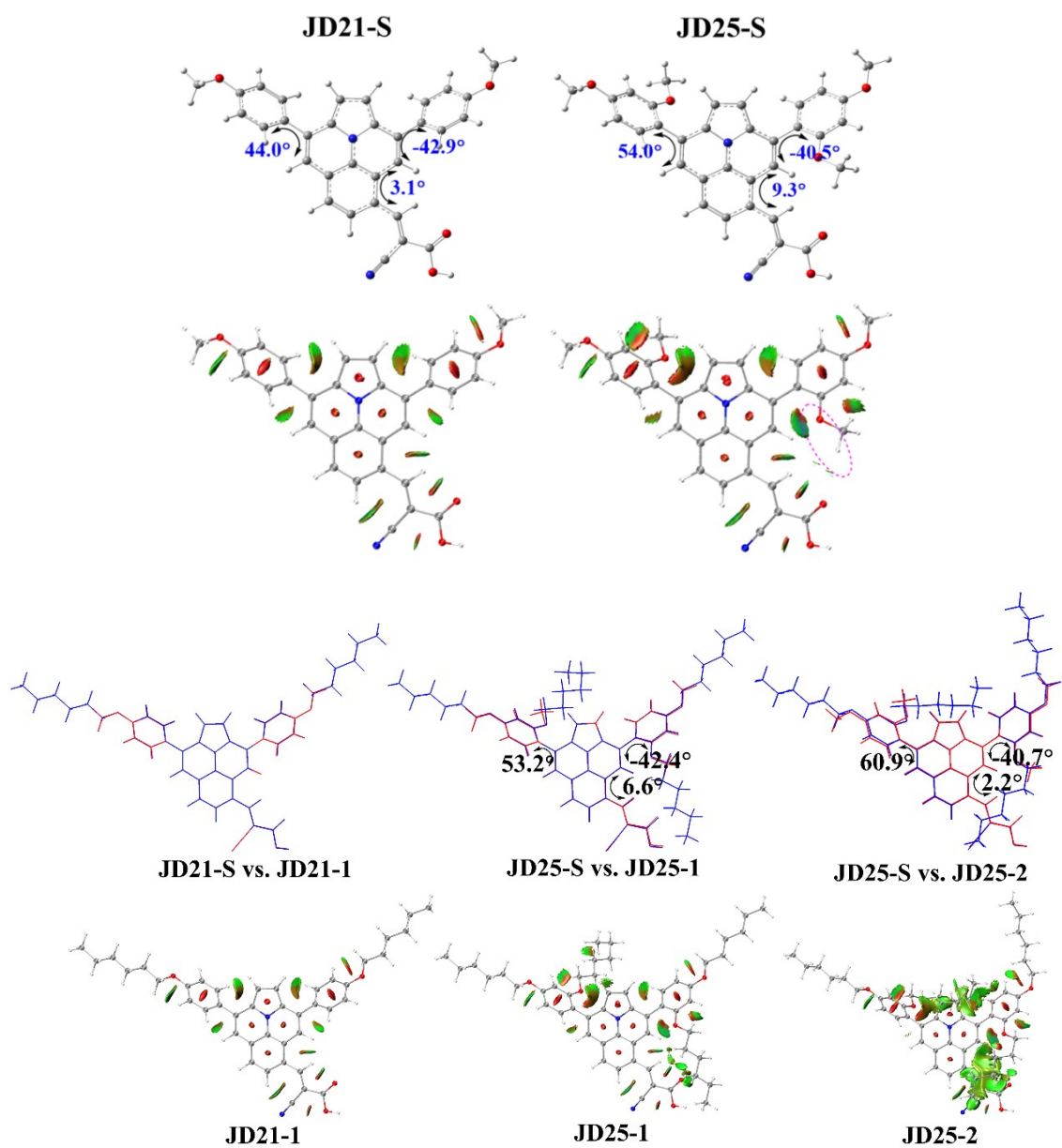Fig. S2 Color scale bar used to represent values of $sign(\lambda_2)\rho$.

Fig. S3 Optimized molecular structures with main dihedral angle, as well as the color-filled RDG map with iso-surface of 0.7 a.u.
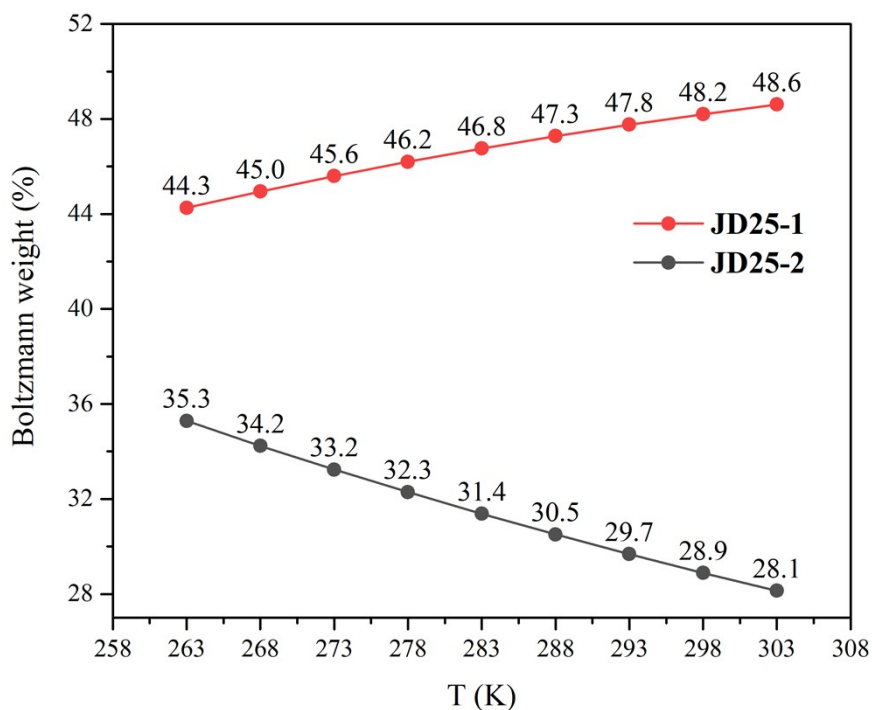
Fig.S4 Variation of Boltzmann weight with temperature for **JD25-1** and **JD25-2**.

Table S1 Calculated thermodynamic values of different conformations of **JD25** at different temperatures.

| T (K)	System	U (a.u.)	H (a.u.)	G (a.u.)	S (J/mol/K)	CV (J/mol/K)	Relative G	Boltzmann weight
263	**JD25-1**	-2656.364	-2656.363	-2656.492	1285.934	891.116	0	44.26%
	JD25-2	-2656.367	-2656.366	-2656.492	1258.315	888.402	0.495	35.29%
268	**JD25-1**	-2656.362	-2656.362	-2656.494	1300.546	905.843	0	44.95%
	JD25-2	-2656.365	-2656.364	-2656.494	1272.979	903.266	0.607	34.24%
273	**JD25-1**	-2656.361	-2656.360	-2656.497	1315.155	920.636	0	45.60%
	JD25-2	-2656.363	-2656.362	-2656.496	1287.641	918.191	0.717	33.24%
278	**JD25-1**	-2656.359	-2656.358	-2656.499	1329.763	935.489	0	46.20%
	JD25-2	-2656.362	-2656.361	-2656.499	1302.302	933.169	0.828	32.29%
283	**JD25-1**	-2656.357	-2656.356	-2656.501	1344.37	950.393	0	46.76%
	JD25-2	-2656.360	-2656.359	-2656.501	1316.964	948.193	0.939	31.38%
288	**JD25-1**	-2656.355	-2656.354	-2656.503	1358.977	965.343	0	47.28%
	JD25-2	-2656.358	-2656.357	-2656.503	1331.628	963.257	1.049	30.51%
293	**JD25-1**	-2656.353	-2656.353	-2656.506	1373.586	980.33	0	47.76%
	JD25-2	-2656.356	-2656.355	-2656.505	1346.294	978.354	1.158	29.68%
298	**JD25-1**	-2656.352	-2656.351	-2656.508	1388.197	995.347	0	48.20%
	JD25-2	-2656.354	-2656.353	-2656.508	1360.963	993.476	1.268	28.89%
303	**JD25-1**	-2656.350	-2656.349	-2656.511	1402.81	1010.387	0	48.61%
	JD25-2	-2656.352	-2656.351	-2656.510	1375.635	1008.616	1.377	28.14%
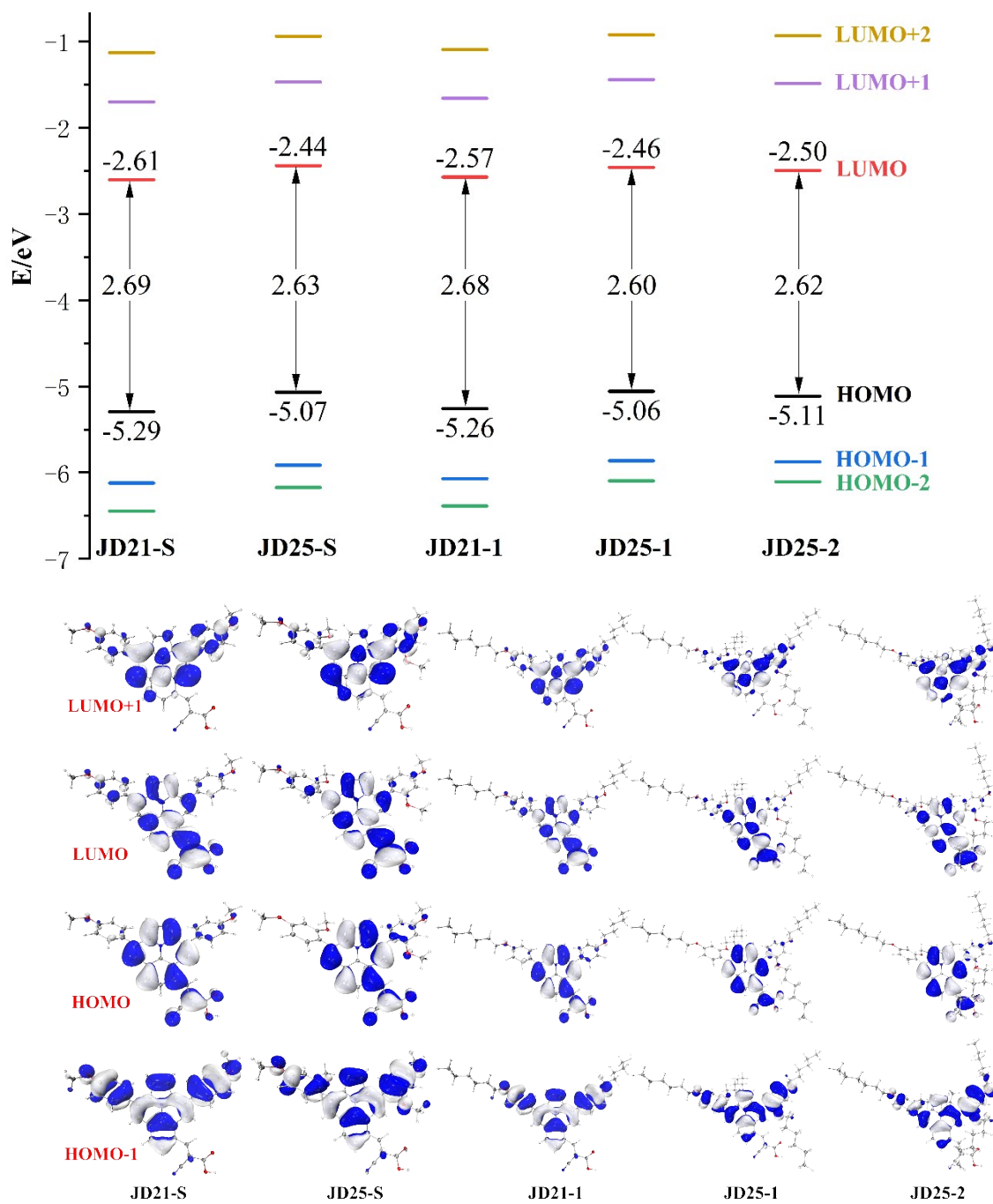
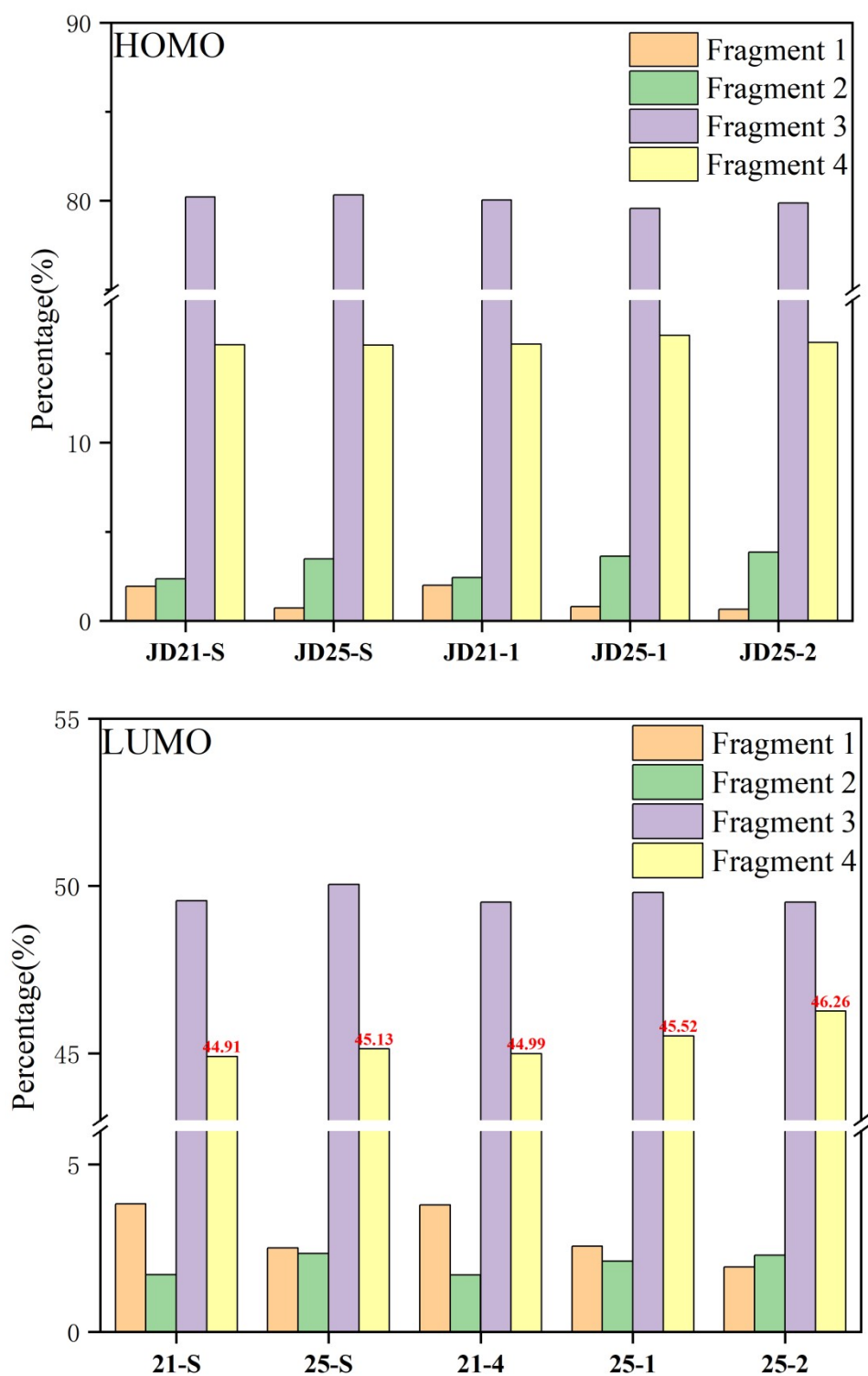Fig.S5 Distributions of frontier molecular orbitals as well as the energies with an isosurface of 0.02 a.u.

Fig. S6 Molecular orbital composition of HOMO and LUMO for these ullazine dyes in terms of each part. (Fragment 1: the left methoxy substituted benzene ring; Fragment 2: the right methoxy substituted benzene ring; Fragment 3: ullazine ring; Fragment 4: cyanoacrylic acid acceptor)

Functional	B3LYP	PBE0	PBE38	M06-2X	CAM-B3LYP	Exp.
Percentage of HF	20%	25%	37.5%	54%	-----	-----
E_x (eV)	2.21	2.26	2.36	2.39	2.40	2.13

Fig. S7 Calculated absorption spectra of **JD21-S** at different functionals in comparison with experimental values.

B3LYP: [35]

PBE0: [36]

PBE38: [37]

M06-2X: [38]

CAM-B3LYP: [39]

Fig. S8 Simulated absorption spectra with oscillator strength (*f*), corresponding computed absorption wavelength (λ_{max}, nm), major transition configuration, hole and electron distributions (isosurface = 0.02 a.u.) as well as the fragment contributions plotted as heat map for visual inspection at TD-PCM-PBE0/6-311G** level in dichloromethane solvent. (Blue regions denote the hole distributions and yellow regions denote the electron distributions. Fragment 1: the left methoxy substituted benzene ring; Fragment 2: the right methoxy substituted benzene ring; Fragment 3: ullazine ring; Fragment 4: cyanoacrylic acid acceptor))
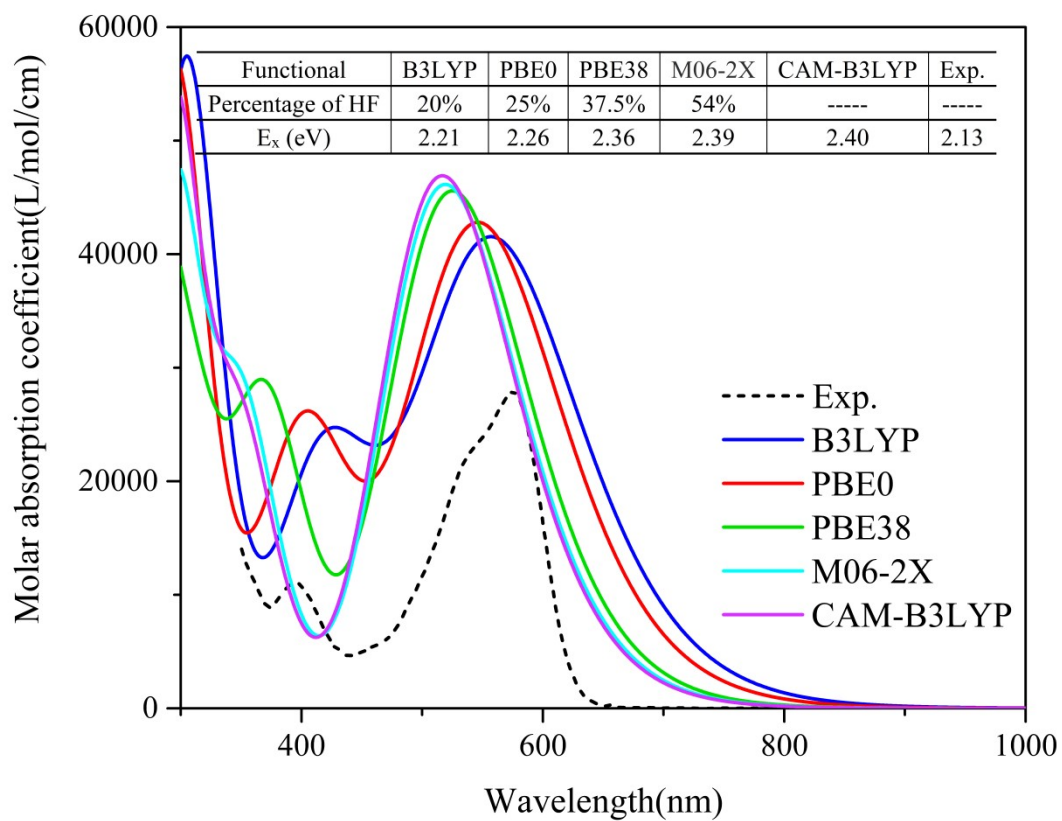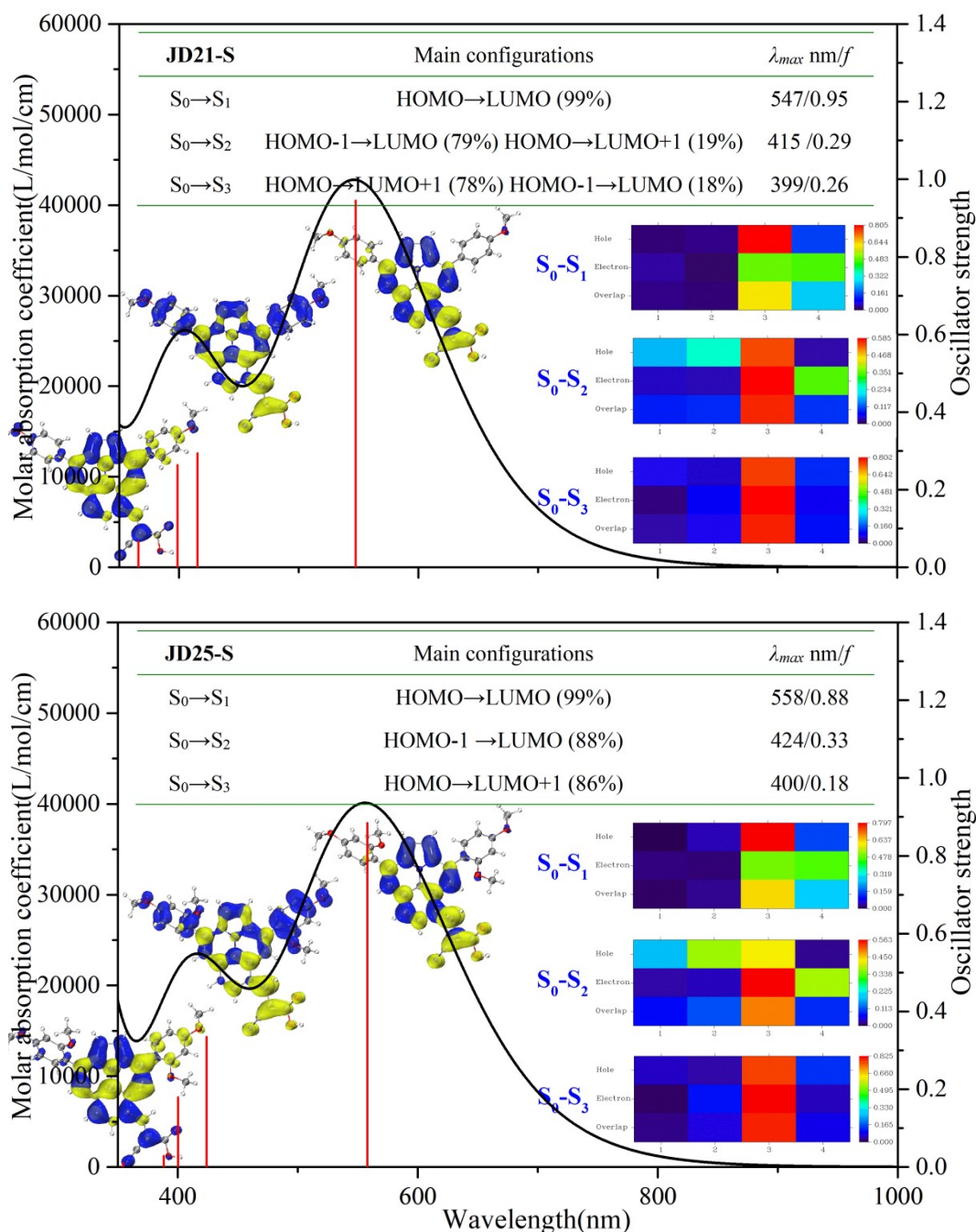
JD21-1

	Main configurations	λ_{max} nm/f
$S_0 \rightarrow S_1$	HOMO→LUMO (99%)	548/0.95
$S_0 \rightarrow S_2$	HOMO-1→LUMO (81%) HOMO→LUMO+1 (16%)	416 /0.32
$S_0 \rightarrow S_3$	HOMO→LUMO+1 (80%) HOMO-1→LUMO (16%)	399/0.26

JD25-1

	Main configurations	λ_{max} nm/f
$S_0 \rightarrow S_1$	HOMO→LUMO (99%)	562/0.89
$S_0 \rightarrow S_2$	HOMO-1→LUMO (91%)	429/0.35
$S_0 \rightarrow S_3$	HOMO→LUMO+1 (85%)	400/0.20

JD25-2

	Main configurations	λ_{max} nm/f
$S_0 \rightarrow S_1$	HOMO→LUMO (99%)	557/0.86
$S_0 \rightarrow S_2$	HOMO-1→LUMO (93%)	430/0.30
$S_0 \rightarrow S_3$	HOMO→LUMO+1 (80%) HOMO-2→LUMO (11%)	399/0.18

Fig. S9 Simulated absorption spectra with oscillator strength (*f*), corresponding computed absorption wavelength (λ_{max}, nm), major transition configuration, hole and electron distributions (isosurface = 0.02 a.u.) as well as the fragment contributions plotted as heat map for visual inspection at TD-PCM-PBE0/6-311G** level in dichloromethane solvent. (Blue regions denote the hole distributions and yellow regions denote the electron distributions. Fragment 1: the left methoxy substituted benzene ring; Fragment 2: the right methoxy substituted benzene ring; Fragment 3: ullazine ring; Fragment 4: cyanoacrylic acid acceptor))
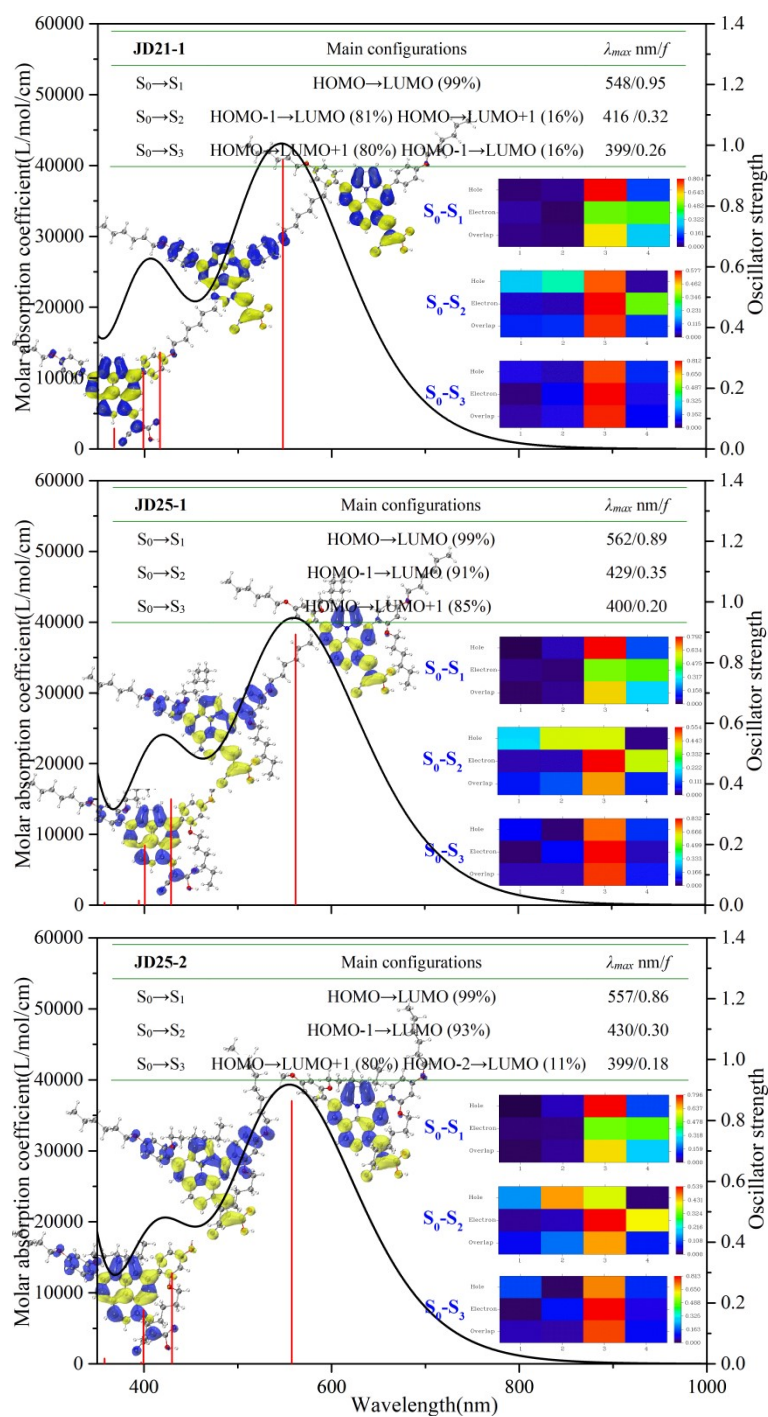
12

Details about the discussion of the hole and electron distributions and heat maps

Although the electron transfer characteristics can be investigated by investigating the hole and electron isosurface map, the image obviously depends on the selection of iso-surface. Therefore, by drawing hole/electron composition as heat map, we can more intuitively reflect the contribution of the fragment to holes and electrons. By viewing color of the matrix elements of these heat maps, we can immediately make clear where the excited electrons come and where they go. At the same time, the contributions of each fragment to electrons and holes are listed in Table S2. We compare the heat maps of **JD21-S** and **JD25-S** to investigate the effect of additional alkoxy groups on the transition properties. We find that the addition of methoxy group have little effect on the transition of S_0-S_1. Holes are mainly distributed on ullazine (fragment 3), while electrons are distributed on ullzine (fragment 3) and cyanoacrylic acid receptors (fragment 4). Methoxy group effects on the transition of S_0-S_3 is mainly reflected in the electron distribution on the receptor, from 8% reduce to 5%. The addition of methoxy group has a great influence on the transition of S_0-S_2. From the heat map, it can be seen that the holes corresponding to this transition are not only distributed on the ullazine and cyanoacrylic acid acceptor, but also on the methoxy substituted benzene rings on the left and right sides, and the electrons are mainly distributed on the ullazine and cyanoacrylic acid acceptor. After the addition of methoxy group, the hole distribution on ullazine fragment decreases from 54% to 43%, and the electron distribution on cyanoacrylic acid increases from 34% to 38%. By comparing Fig. 11 and Fig. 12, we can explore the influence of alkyl chain simplification on the transition properties of dyes. We find that there is almost no change for **JD21-1** as compared with **JD21-S**, and the same as **JD25-1** versus **JD25-S**. Compared with the simplified dyes, the S_0-S_2 and S_0-S_3 transitions of **JD25-2** change a lot. For the S_0-S_2 transition, the hole distribution on the ullazine fragment decreases and the electron distribution on the cyanoacrylic acid increases from 38% to 40% after the alkyl chain grows. For the S_0-S_3 transition, the electron distribution on cyanoacrylic acid acceptor increases from 5% to 7%, as high as **JD21-1**. According to the working principle of DSSCs, we know that the more electrons distributed on the acceptor group, the more electrons injected into the

conduction band of the semiconductor after light excitation, so as to improve the efficiency of the device. In general, through the analysis of the transition properties of these dyes, we get the conclusion that when there is a strong interaction between alkyl chain and dye molecules, it will have a certain impact on the electronic structure of dyes, especially the electron distributions on the acceptor group after light excitation.

Table S2 Calculated contributions of each fragment to hole and electron distributions upon photoexcitation.

| Dye	transition	h^+/e^-	1	2	3	4
21-S	$S_0{\rightarrow}S_1$	Hole	1.95	2.82	80.51	14.72
		Electron	3.56	1.40	48.73	**46.31**
	$S_0{\rightarrow}S_2$	Hole	17.89	24.97	54.27	2.87
		Electron	3.91	3.36	58.54	**34.18**
	$S_0{\rightarrow}S_3$	Hole	6.84	5.46	75.32	12.39
		Electron	2.43	9.05	80.23	**8.29**
25-S	$S_0{\rightarrow}S_1$	Hole	0.74	4.67	79.68	14.91
		Electron	2.40	1.97	49.50	**46.12**
	$S_0{\rightarrow}S_2$	Hole	17.56	37.13	43.27	2.04
		Electron	2.86	3.34	56.30	**37.50**
	$S_0{\rightarrow}S_3$	Hole	5.47	3.98	77.07	13.48
		Electron	1.40	10.91	82.51	**5.18**
21-1	$S_0{\rightarrow}S_1$	Hole	1.97	2.86	80.40	14.77
		Electron	3.54	1.39	48.78	**46.28**
	$S_0{\rightarrow}S_2$	Hole	18.73	25.99	52.68	2.60
		Electron	3.95	3.21	57.75	**35.09**
	$S_0{\rightarrow}S_3$	Hole	6.43	4.91	75.98	12.68
		Electron	2.42	9.14	81.19	**7.25**
25-1	$S_0{\rightarrow}S_1$	Hole	0.81	4.56	79.21	15.42
		Electron	2.55	1.95	49.65	**45.84**
	$S_0{\rightarrow}S_2$	Hole	19.16	39.33	39.76	1.75
		Electron	2.99	3.08	55.39	**38.54**
	$S_0{\rightarrow}S_3$	Hole	9.52	2.09	74.65	13.75
		Electron	1.93	9.90	83.20	**4.97**
25-2	$S_0{\rightarrow}S_1$	Hole	0.61	4.78	79.62	14.99
		Electron	2.01	2.22	49.08	**46.68**
	$S_0{\rightarrow}S_2$	Hole	14.25	45.77	38.58	1.40
		Electron	2.31	3.36	53.92	**40.42**
	$S_0{\rightarrow}S_3$	Hole	15.07	1.57	70.76	12.60
		Electron	1.34	10.65	81.28	**6.73**
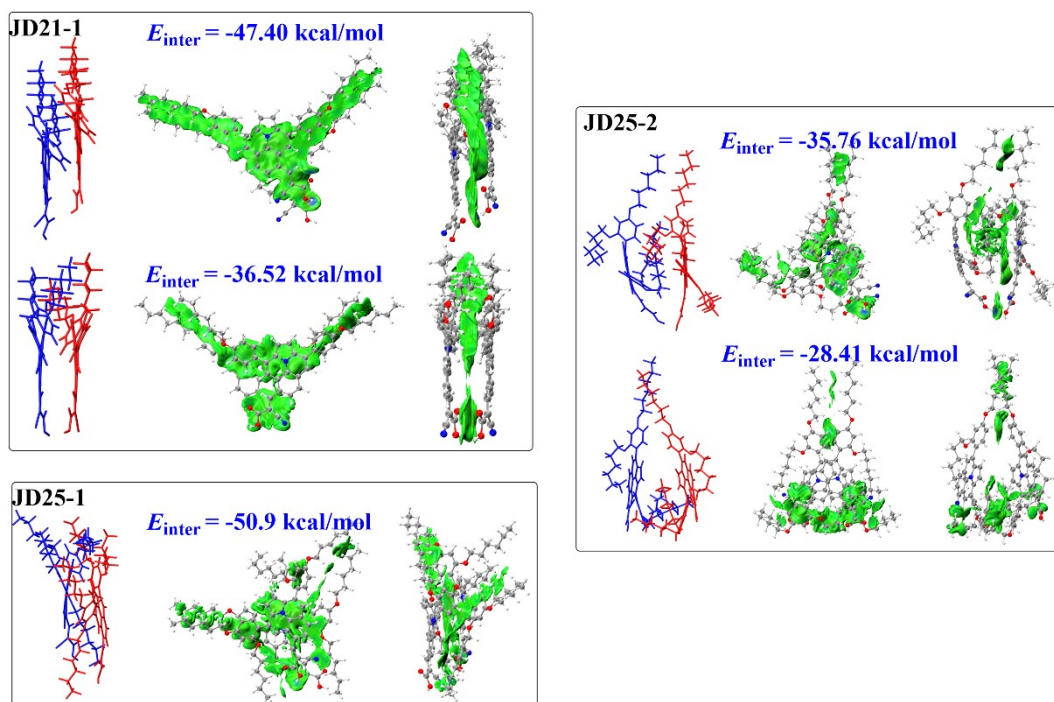
Fig. S10 Optimized geometries of the dyes in face-to-face configurations as well as the interaction energies at B3LYP-D3(BJ)/6-311G** with BSSE correction and $sign(\lambda_2)\rho$ colored isosurfaces of δg^{inter} = 0.002 a.u. corresponding to IGMH analyses.

Detailed discussion:

For the dimer formed by **JD21-1** and **JD25-1**, because the alkyl chain is in an extended state, it has little effect on the conjugate system of the dye molecular, the E_{inter} comes from the π-π interaction between the conjugated fragments and vdW interaction between the alkyl chain and the alkyl chain. For **JD25-2**, since the π-π interaction of the conjugate fragment is effectively avoided due to the addition of the alkyl chain, which is wound on the molecular skeleton, the E_{inter} mainly comes from the vdW interaction between the alkyl chain and the alkyl chain.
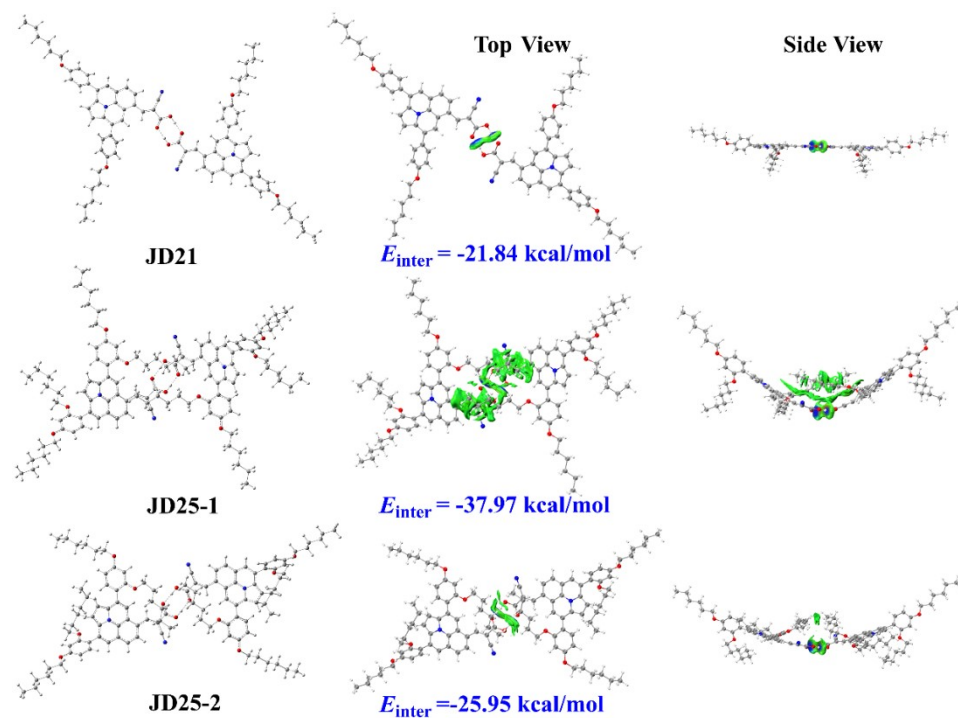
	Top View	Side View
JD21	E_{inter} = -21.84 kcal/mol	
JD25-1	E_{inter} = -37.97 kcal/mol	
JD25-2	E_{inter} =-25.95 kcal/mol	

Fig. S11 Optimized geometries of the dyes in tail-to-tail configurations as well as the interaction energies at B3LYP-D3(BJ)/6-311G** with BSSE correction and $sign(\lambda_2)\rho$ colored isosurfaces of δg^{inter} = 0.002 a.u. corresponding to IGMH analyses.
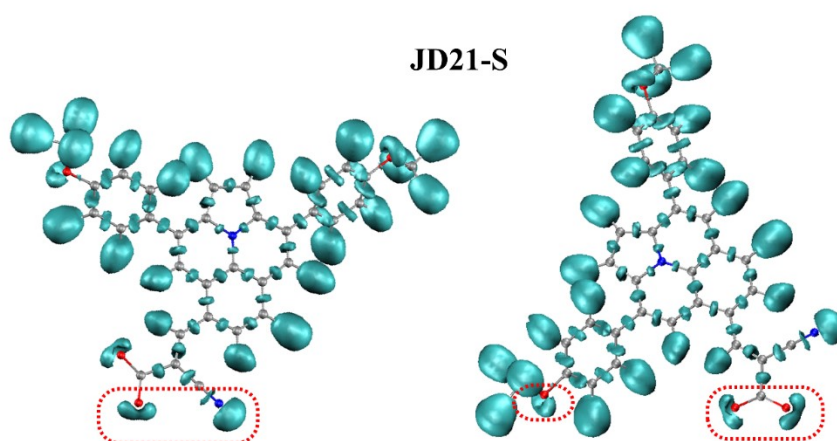

JD21-S

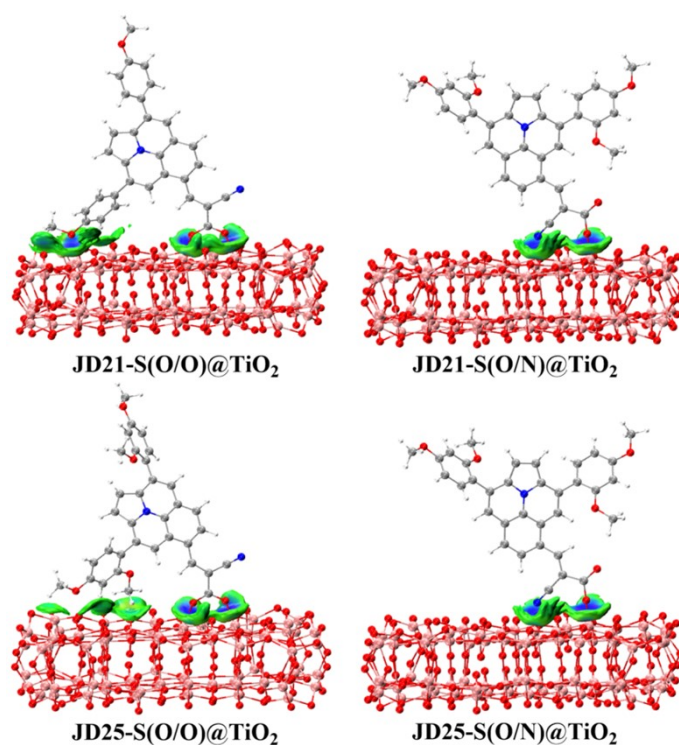Fig. S12 The ELF with isosurface of 0.87 a.u. for dissociated **JD21-S**.

Fig. S13 $sign(\lambda_2)\rho$ colored isosurfaces of δg^{inter} = 0.002 a.u. corresponding to IGMH analyses.
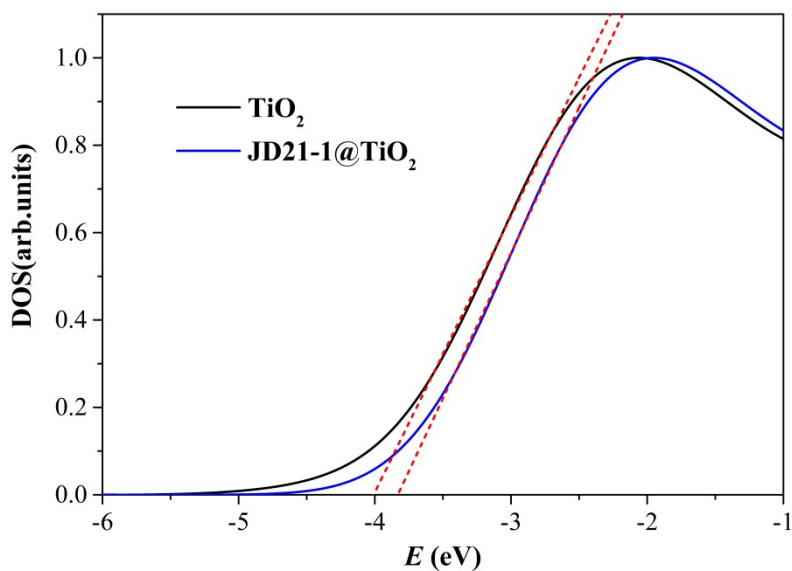

Fig. S14 Total and Partial Density of States (DOS) for **JD21-1** adsorbed on $(TiO_2)_{82}$ cluster. (black solid line) $(TiO_2)_{82}$ cluster DOS, (blue dash line) PDOS, $(TiO_2)_{48}$ cluster contribution to the total DOS. The red solid lines intercepts with the energy axis correspond to the calculated CB edges.
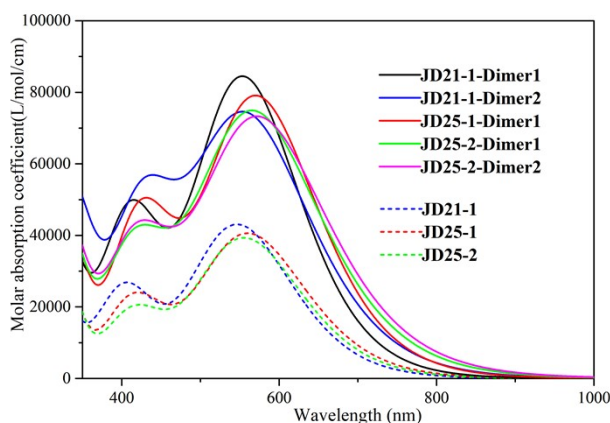
Fig. S15 Simulated absorption spectra for the monomers (dotted line) and dimers (solid line) using Gaussian function with a full width at half-maximum (FWHM) of 0.3 eV to broaden the theoretically calculated data as spectrum curve.

Table S3 The computed maximum absorption wavelengths (λ_{max}), oscillator strengths (*f*), major transition configuration of these dimers.

| 21-1-Dimer1	Main configuration	λ_{max}nm/f
$S_0 \rightarrow S_3$	HOMO-1→LUMO (63%) HOMO→LUMO+1(34%)	555/1.71
$S_0 \rightarrow S_6$	HOMO-3→LUMO (59%) HOMO-1→LUMO+2(13%)	423/0.32
$S_0 \rightarrow S_8$	HOMO-1→LUMO+2(30%) HOMO-1→LUMO+3(24%)	409/0.44
21-1-Dimer2	Main configuration	λ_{max}nm/f
$S_0 \rightarrow S_4$	HOMO-1→LUMO+1(89%)	544/1.09
$S_0 \rightarrow S_6$	HOMO-2→LUMO (52%) HOMO→LUMO+2(17%)	441/0.49
$S_0 \rightarrow S_{10}$	HOMO-3→LUMO+1(70%) HOMO→LUMO+3(20%)	418/0.34
25-1-Dimer1	Main configuration	λ_{max}nm/f
$S_0 \rightarrow S_2$	HOMO→LUMO+1(60%) HOMO-1→LUMO (34%)	572/1.54
$S_0 \rightarrow S_6$	HOMO-3→LUMO+1(71%) HOMO-2→LUMO+1(13%)	435/0.41
$S_0 \rightarrow S_7$	HOMO-1→LUMO+2 (86%) HOMO-2→LUMO (9%)	414/0.18
25-2-Dimer1	Main configuration	λ_{max}nm/f
$S_0 \rightarrow S_2$	HOMO-1→LUMO+1(78%) HOMO→LUMO (21%)	569/1.65
$S_0 \rightarrow S_6$	HOMO-3→LUMO (85%) HOMO→LUMO+2(12%)	430/0.33
$S_0 \rightarrow S_8$	HOMO-1→LUMO+3(86%) HOMO-2→LUMO+1(8%)	408/0.21
25-2-Dimer2	Main configuration	λ_{max}nm/f
$S_0 \rightarrow S_1$	HOMO→LUMO (99%)	580/0.87
$S_0 \rightarrow S_2$	HOMO-1→LUMO+1(98%)	572/0.91
$S_0 \rightarrow S_6$	HOMO-3→LUMO+1(87%) HOMO-1→LUMO+3(10%)	433/0.30
$S_0 \rightarrow S_8$	HOMO-1→LUMO+3(83%)HOMO-3→LUMO+1(11%)	409/0.25
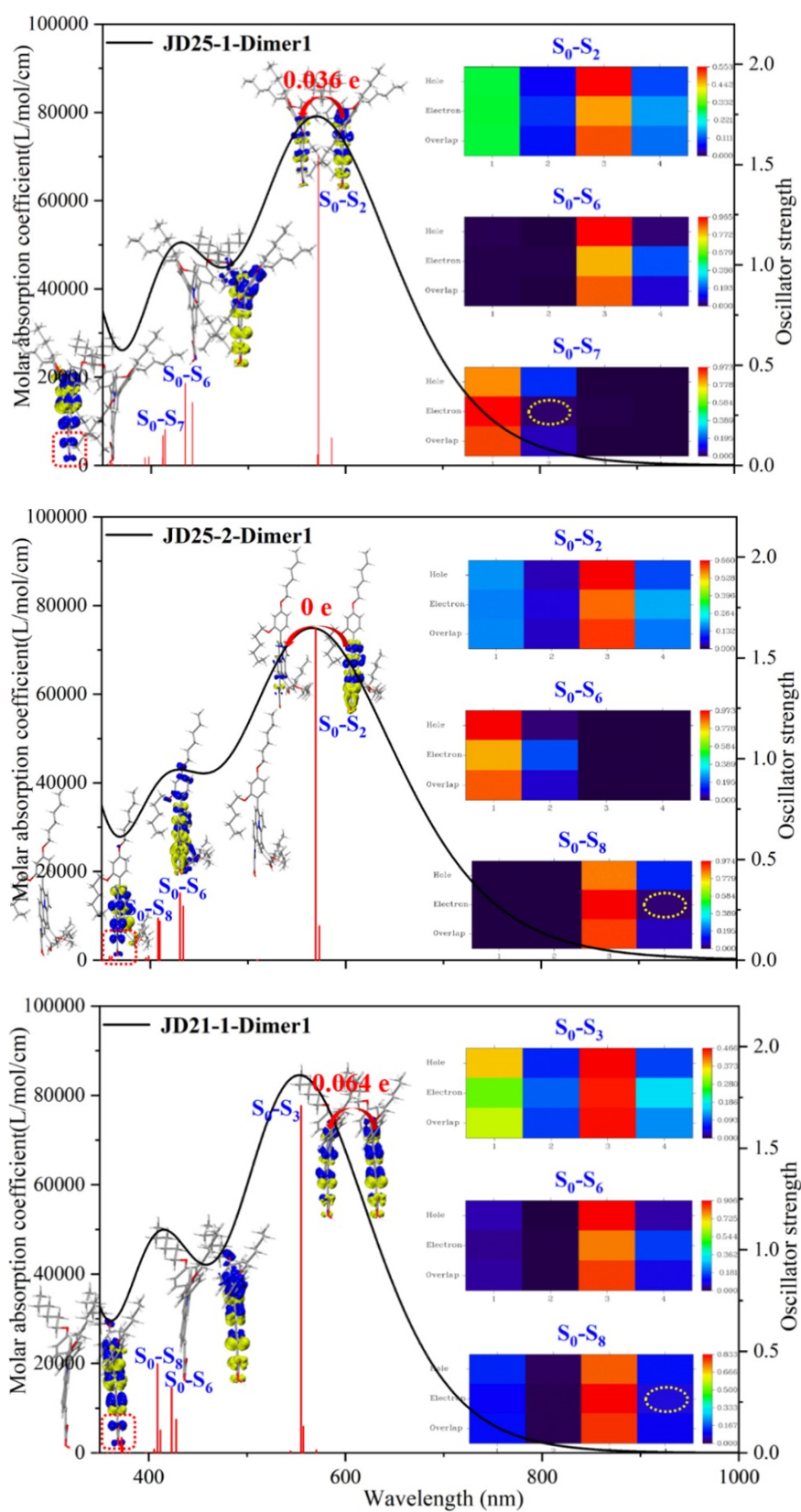
Fig. S16 Simulated absorption spectra with oscillator strength (*f*), hole and electron distributions (isosurface = 0.02 a.u.) with the amount of electron transfer for the transition at the maximum

absorption peak as well as the fragment contributions plotted as heat map at TD-PCM-PBE0/6-311G** level in dichloromethane solvent. (Blue regions denote the hole distributions and yellow regions denote the electron distributions. For each dimer, four fragments are defined in the following way. Each monomer in the dimer is divided into two pieces, with phenyl substituted ullazine in the left monomer as fragment 1, cyanoacrylic acid as fragment 2, phenyl substituted ullazine in the right monomer as fragment 3 and cyanoacrylic acid as fragment 4.)

Table S4 Calculated contributions of each fragment to hole and electron distributions upon photoexcitation.

Dimer	transition	h^+/e^-	1	2	3	4
JD21-1-Dimer1	$S_0 \rightarrow S_3$	Hole	37.51	7.13	46.62	8.75
		Electron	28.29	**9.96**	45.48	**16.28**
	$S_0 \rightarrow S_6$	Hole	4.83	0.23	90.59	4.34
		Electron	3.40	**0.62**	79.62	**16.36**
	$S_0 \rightarrow S_8$	Hole	12.48	1.12	75.56	10.84
		Electron	8.91	**0.75**	83.27	**7.07**
JD21-1-Dimer2	$S_0 \rightarrow S_4$	Hole	45.87	6.30	41.80	6.03
		Electron	49.38	**15.89**	27.21	**7.52**
	$S_0 \rightarrow S_6$	Hole	63.18	4.81	30.86	1.64
		Electron	54.83	**8.66**	28.82	**7.69**
	$S_0 \rightarrow S_{10}$	Hole	40.64	2.75	54.21	2.41
		Electron	60.29	**13.15**	23.71	**2.84**
JD25-1-Dimer1	$S_0 \rightarrow S_2$	Hole	28.29	5.87	55.25	10.59
		Electron	28.69	**9.21**	46.70	**15.41**
	$S_0 \rightarrow S_6$	Hole	0.84	0.02	96.53	2.61
		Electron	0.66	**0.50**	79.53	**19.32**
	$S_0 \rightarrow S_7$	Hole	84.18	15.57	0.22	0.03
		Electron	97.27	**2.25**	0.49	**0.00**
JD25-2-Dimer1	$S_0 \rightarrow S_2$	Hole	17.58	3.73	66.05	12.64
		Electron	16.18	**5.14**	59.26	**19.42**
	$S_0 \rightarrow S_6$	Hole	97.29	2.48	0.23	0.00
		Electron	80.90	**18.88**	0.17	**0.05**
	$S_0 \rightarrow S_8$	Hole	0.19	0.04	85.54	14.22
		Electron	**0.27**	**0.00**	97.37	**2.35**
JD25-2-Dimer2	$S_0 \rightarrow S_1$	Hole	0.00	-0.00	82.69	17.30
		Electron	0.01	**0.00**	76.17	**23.82**
	$S_0 \rightarrow S_2$	Hole	83.14	16.85	0.00	0.00
		Electron	76.50	**23.51**	-0.00	**-0.00**
	$S_0 \rightarrow S_6$	Hole	98.01	2.12	-0.13	-0.00
		Electron	80.77	**19.25**	-0.01	**-0.00**
	$S_0 \rightarrow S_8$	Hole	85.19	14.61	0.16	0.04

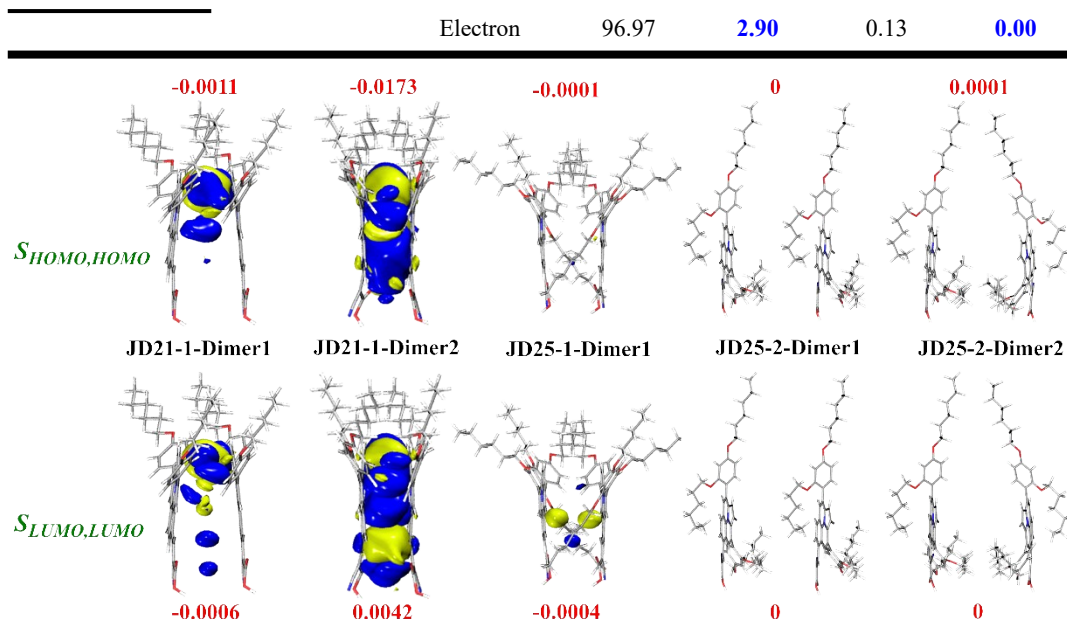|	Electron	96.97	**2.90**	0.13	**0.00**

Fig. S17 HOMO-HOMO and LUMO-LUMO overlap between the two monomers for each dimer with isosurface of 0.000006 a.u. The red font is the overlap integral.

References

1. Tian Lu, molclus program, Version 1.9.9.9, http://www.keinsci.com/research/molclus.html.
2. C. Bannwarth, E. Caldeweyher, S. Ehlert, A. Hansen, P. Pracht, J. Seibert, S. Spicher and S. Grimme, *WIREs Computational Molecular Science*, 2021, **11**, e1493.
3. S. Grimme, C. Bannwarth and P. Shushkov, *J. Chem. Theory Comput.*, 2017, **13**, 1989-2009.
4. C. Bannwarth, S. Ehlert and S. Grimme, *J. Chem. Theory Comput.*, 2019, **15**, 1652-1671.
5. S. Grimme, *J. Chem. Theory Comput.*, 2019, **15**, 2847-2862.
6. P. Pracht and S. Grimme, *Chem. Sci.*, 2021, **12**, 6551-6568.
7. P. Pracht, F. Bohle and S. Grimme, *Phys. Chem. Chem. Phys.*, 2020, **22**, 7169-7192.
8. L. Goerigk and S. Grimme, *J. Chem. Theory Comput.*, 2011, **7**, 291-309.
9. G. A. Petersson and M. A. Al-Laham, *J.Chem. Phys.*, 1991, **94**, 6081-6090.
10. F. Weigend, *Phys. Chem. Chem. Phys.*, 2006, **8**, 1057-1065.
11. A. V. Marenich, C. J. Cramer and D. G. Truhlar, *J. Phys. Chem. B*, 2009, **113**, 6378-6396.
12. F. Neese, *WIREs Computational Molecular Science*, 2018, **8**, e1327.
13. F. Neese, *WIREs Computational Molecular Science*, 2012, **2**, 73-78.
14. F. Neese, F. Wennmohs, U. Becker and C. Riplinger, *J.Chem. Phys.*, 2020, **152**, 224108.
15. T. Lu and Q. Chen, *Computational and Theoretical Chemistry*, 2021, **1200**, 113249.
16. S. Grimme, *Chemistry – A European Journal*, 2012, **18**, 9955-9964.
17. P. Persson, R. Bergström and S. Lunell, *J. Phys. Chem. B*, 2000, **104**, 10348-10351.
18. F. De Angelis, A. Tilocca and A. Selloni, *J. Am. Chem. Soc.*, 2004, **126**, 15024-15025.
19. P. Ordejón, E. Artacho and J. M. Soler, *Physical Review B - Condensed Matter and Materials Physics*, 1996, **53**, R10441-R10444.
20. D. Sánchez-Portal, P. Ordejón, E. Artacho and J. M. Soler, *Int. J. Quantum Chem.*, 1997, **65**, 453-461.

21. M. S. José, A. Emilio, D. G. Julian, G. Alberto, J. Javier, O. Pablo and S.-P. Daniel, *J. Phys.: Condens. Matter*, 2002, **14**, 2745.

22. J. P. Perdew, K. Burke and M. Ernzerhof, *Phys. Rev. Lett.*, 1996, **77**, 3865-3868.

23. S. Grimme, *J. Comput. Chem.*, 2006, **27**, 1787-1799.

24. R. o. Sánchez-de-Armas, J. Oviedo López, M. A. San-Miguel, J. F. Sanz, P. Ordejón and M. Pruneda, *J. Chem. Theory Comput.*, 2010, **6**, 2856-2865.

25. R. o. Sánchez-de-Armas, J. Oviedo, M. A. n. San Miguel and J. F. Sanz, *J. Phys. Chem. C*, 2011, **115**, 11293-11301.

26. S. Meng and E. Kaxiras, *Nano Lett.*, 2010, **10**, 1238-1247.

27. J. Feng, Y. Jiao, W. Ma, M. K. Nazeeruddin, M. Grätzel and S. Meng, *J. Phys. Chem. C*, 2013, DOI: 10.1021/jp310504n.

28. R. Sánchez-de-Armas, M. Á. San Miguel, J. Oviedo and J. F. Sanz, *Phys. Chem. Chem. Phys.*, 2012, **14**, 225-233.

29. J. Zhang, H.-B. Li, J.-Z. Zhang, Y. Wu, Y. Geng, Q. Fu and Z.-M. Su, *J. Mater. Chem. A*, 2013, **1**, 14000-14007.

30. J. Zhang, C.-J. Chen and H.-C. Zhu, *Appl. Surf. Sci.*, 2020, **513**, 145844.

31. H.-C. Zhu, C.-F. Li, Z.-H. Fu, S.-S. Wei, X.-F. Zhu and J. Zhang, *Appl. Surf. Sci.*, 2018, **455**, 1095-1105.

32. H.-C. Zhu, J. Zhang and Y.-L. Wang, *Appl. Surf. Sci.*, 2018, **433**, 1137-1147.

33. E. R. Johnson, S. Keinan, P. Mori-Sánchez, J. Contreras-García, A. J. Cohen and W. Yang, *J. Am. Chem. Soc.*, 2010, **132**, 6498-6506.

34. T. Lu and Q. Chen, *J. Comput. Chem.*, 2022, **43**, 539-555.

35. A. D. Becke, *J. Chem. Phys.*, 1993, **98**, 5648-5652.

36. C. Adamo and V. Barone, *J. Chem. Phys.*, 1999, **110**, 6158-6170.

37. S. Grimme, J. Antony, S. Ehrlich and H. Krieg, *J. Chem. Phys.*, 2010, **132**, 154104.

38. Y. Zhao and D. G. Truhlar, *Theor. Chem. Acc.*, 2008, **120**, 215-241.

39. T. Yanai, D. P. Tew and N. C. Handy, *Chem. Phys. Lett.*, 2004, **393**, 51-57.